EPJ manuscript No.
(will be inserted by the editor)

Hyperon-mixed neutron star with universal many-body repulsion

Y. Yamamoto[1], T. Furumoto[2], N. Yasutake[3] and Th.A. Rijken[4]

[1] Nishina Center for Accelerator-Based Science, Institute for Physical and Chemical Research (RIKEN), Wako, Saitama, 351-0198, Japan
[2] National Institute of Technology, Ichinoseki College, Ichinoseki, Iwate, 021-8511, Japan
[3] Department of Physics, Chiba Institute of Technology, 2-1-1 Shibazono Narashino, Chiba 275-0023, Japan
[4] IMAPP, University of Nijmegen, Nijmegen, The Netherlands

Received: date / Revised version: date

Abstract. Neutron stars with large masses $\sim 2M_\odot$ require the hard stiffness of equation of state (EoS) of neutron-star matter. On the other hand, hyperon mixing brings about remarkable softening of EoS. In order to solve this problem, a multi-pomeron exchange potential (MPP) is introduced as a model for the universal many-body repulsion in baryonic systems on the basis of the Extended Soft Core (ESC) baryon-baryon interaction. The strength of MPP is determined by analyzing the nucleus-nucleus scattering with the G-matrix folding model. The interactions in ΛN, ΣN and ΞN channels are shown to be consistent with experimental indications. The EoS in neutron-star matter with hyperon mixing is obtained from ESC in addition of MPP, and mass-radius relations of neutron stars are derived. The maximum mass is shown to reach $2M_\odot$ even in the case of including hyperon mixing on the basis of model-parameters determined by terrestrial experiments.

PACS. 21.65.Cd 21.80.+a 25.70.-z 26.60.Kp

1 Introduction

The observed masses of neutron stars J1614-2230 [1] and J0348-0432 [2] are given as $(1.97 \pm 0.04)M_\odot$ and $(2.01 \pm 0.04)M_\odot$, respectively. These large masses give a severe condition for the stiffness of equation of state (EoS) of neutron-star matter. It is well known that the stiff EoS giving the maximum mass of $2M_\odot$ can be derived from the existence of strong three-nucleon repulsion (TNR) in the high-density region. However, the hyperon (Y) mixing in neutron-star matter brings about the remarkable softening of the EoS, which cancels the TNR effect for the maximum mass [3,4,5].

One of ideas to avoid this serious problem, called "Hyperon puzzle in neutron stars", is to consider that the TNR-like repulsions work universally for YNN, YYN YYY as well as for NNN [5]. In our previous works [6,7], we introduced the multi-pomeron exchange potential (MPP) as a model of universal repulsions among three and four baryons on the basis of the Extended Soft Core (ESC) baryon-baryon interaction model developed by two of authors (T.R. and Y.Y.) and M.M. Nagels [8,9,10,11]. Here, the Brueckner-Hartree-Fock (BHF) formalism was used to derive the EoS of neutron-star matter including hyperons (Λ and Σ^-).

The most important point in such a work is how to determine the strength parameters related to for the stiffness of EoS: In our approach, those of MPP were determined on the basis of terrestrial experiments, introducing no ad hoc parameter for the stiffness. Usually, it is considered that some information on the incompressibility K of high-density matter can be extracted from analyses of central heavy-ion collisions in high energies. In the present, however, the results for the EoS still remain inconclusive. On the other hand, in [6,7] we used the result that the TNR effect appeared in the experimental angular distributions of ^{16}O+^{16}O elastic scattering (E/A=70 MeV), as shown in [12,13]: Such a scattering phenomenon was analyzed successfully with the complex G-matrix folding potentials derived from ESC free-space NN interactions including MPP contributions, where the strengths of MPP are adjusted so as to reproduce the experimental data.

As well known, the nuclear saturation property of the density and energy per particle cannot be reproduced only with use of two-body interactions. It is indispensable to take into account the three-nucleon interaction composed of the attractive part (TNA) and the TNR [14]. When we introduce the MPP, the TNA is added phenomenologically so as to reproduce the nuclear saturation property precisely.

Our interaction model composed of ESC, MPP and TNA is extended to hyperon channels: ESC gives potentials in $S = -1$ (ΛN, ΣN) and $S = -2$ (ΞN, $\Lambda\Lambda$ and $\Lambda\Sigma$) channels. MPP is universal in all BB channels according to its modeling. TNA is given phenomenologically in NN

Send offprint requests to:

channels, which should be taken to reproduce hypernuclear data in hyperonic channels. Thus, we have a three-baryon attraction (TBA). The decisive role for stiffness of EoS and neutron-star mass is played by the MPP part. The existence of high-density strong repulsions in hyperon channels is an assumption to avoid the softening of EoS by hyperon mixing in neutron-star matter. Such an assumption is modeled by MPP in a clear-cut way. Then, the strength of MPP should be determined so as to be consistent with the terrestrial experimental data.

Using our *BB* interaction model (ESC+MPP+TBA), we derive the EoS of β-stable neutron-star matter composed of neutrons (n), protons (p), electrons (e^-), muons (μ^-) and hyperons (Λ, Σ^-, Ξ^-), and solve the Tolmann-Oppenheimer-Volkoff (TOV) equation for the hydrostatic structure to obtain mass-radius relations of neutron stars.

The first step in this paper is to find the parameter sets for MPP and TNA in *NN* channels on the basis of the G-matrix calculations for nucleon matter. The nucleus-nucleus potentials are derived by folding the G-matrix interactions consistent with nuclear saturation properties. The MPP parameters are chosen so as to reproduce the ^{16}O+^{16}O scattering data at E/A=70 MeV. In the nuclear matter calculations, a three-body interaction is replaced approximately to an effective two-body interaction by integrating out a third particle.

The second step is to derive the EoS for neutron-star matter including hyperons (Λ, Σ^-), and to obtain the mass-radius relations of neutron stars by solving the TOV equation. Though the calculations were performed in [7], the obtained stiffness of the EoS was found to be slightly over-estimated due to some insufficiency in numerical calculations. The correct results are given in this work.

The third step is to study the effect of Ξ^- mixing, which was not taken into account in [7]. In this relation, it is important that recently the event of Ξ^- bound state was found in emulsion and the $\Xi-$ binding energy B_{Ξ^-} was extracted [15]. The $S=-2$ sector of ESC reproduces nicely the observed value of B_{Ξ^-}. Then, we derive the EoS of neutron-star matter including Ξ^- together with Λ and Σ^-, and evaluate the effect of Ξ^- mixing to the mass-radius relations of neutron stars.

The paper is organized as follows: In section 2, the strengths of MPP and TBA in nucleonic channels are determined to reproduce the angular distributions of ^{16}O+^{16}O scattering at E/A=70 MeV and the nuclear saturation property. The EoS is derived from a mixed matter of n, p, e and μ in chemical equilibrium, and the mass-radius relations of neutron stars are obtained. In section 3, the EoS is derived from a baryonic matter including not only nucleons but also hyperons (Λ and Σ^-). In spite of substantial softening of the EoS by hyperon mixing, the resultant values of maximum masses of neutron stars reach to $2M_\odot$ owing to the contributions of quartic pomeron exchange terms. The effects of Ξ^- mixing are also investigated. The conclusions of this work are given in section 4.

2 EoS and neutron-star mass

2.1 Multi-pomeron repulsion

We start the *BB* interaction model ESC, where all available *NN*-, *YN*-, and *YY*-data are fitted simultaneously with single sets of meson parameters. Here, two-meson and meson-pair exchanges are taken into account explicitly and no effective boson is included differently from the usual one-boson exchange models. The latest version of ESC model is named as ESC08c [9,10,11]. Hereafter, ESC means this version.

As a model of universal TBR, we introduce the multi-pomeron exchange potential (MPP) [6,7] consistently with the ESC modeling: Generally, the N-body local potential by pomeron exchange is

$$W^{(N)}(\mathbf{x}_1,...,\mathbf{x}_N) = g_P^{(N)} g_P^N \left\{ \int \frac{d^3k_i}{(2\pi)^3} e^{-i\mathbf{k}_i\cdot\mathbf{x}_i} \right\} \cdot \times (2\pi)^3 \delta(\sum_{i=1}^{N} \mathbf{k}_i) \Pi_{i=1}^N \left[\exp\left(-\mathbf{k}_i^2\right)\right] \cdot \mathcal{M}^{4-3N}, \quad (1)$$

where the (low-energy) pomeron propagator is the same as used in the two-body pomeron potential. Since the pomeron is an SU(3)-singlet, MPP's work universally among baryons. The effective two-body potential in a baryonic medium is obtained by integrating over the coordinates $\mathbf{x}_3,...,\mathbf{x}_N$. This gives

$$V_{eff}^{(N)}(\mathbf{x}_1,\mathbf{x}_2) = \rho^{N-2} \int d^3x_3 ... \int d^3x_N \; W^{(N)}(\mathbf{x}_1,\mathbf{x}_2,...,\mathbf{x}_N) = g_P^{(N)} g_P^N \frac{\rho^{N-2}}{\mathcal{M}^{3N-4}} \cdot \frac{1}{\pi\sqrt{\pi}} \left(\frac{m_P}{\sqrt{2}}\right)^3 \exp\left(-\frac{1}{2} m_P^2 r_{12}^2\right). \quad (2)$$

We assume that the dominant mechanism is triple and quartic pomeron exchange. The values of the two-body pomeron strength g_P and the pomeron mass m_P are the same as those in ESC. A scale mass $\mathcal{M}$ is taken as a proton mass.

In order to reproduce the nuclear saturation property, an adequate form of TNA must be added to ESC together with MPP. Here, we introduce TNA phenomenologically as a density-dependent two-body interaction

$$V_A(r;\rho) = V_0 \, \exp(-(r/2.0)^2) \, \rho \, \exp(-\eta\rho) \, (1+P_r)/2 \;, \quad (3)$$

P_r being a space-exchange operator. Here, the functional form is taken to be similar to the TNA part given in [14]. V_0 and η are treated as adjustable parameters. $V_A(r;\rho)$ works only in even states due to the $(1+P_r)$ factor. This assumption is needed to reproduce the ^{16}O+^{16}O potential at $E/A=70$ MeV and nuclear-matter energy consistently [7].

2.2 G-matrix calculation and determination of MPP strength

The lowest-order Bruckner G-matrix calculations with the continuous (CON) choice for intermediate single particle

Table 1. Values of parameters included in MPP and TNA.

	$g_P^{(3)}$	$g_P^{(4)}$	V_0	η
MPa	2.34	30.0	−32.8	3.5
MPa$^+$	1.31	80.0	−21.6	1.0
MPb	2.94	0.0	−45.0	5.4

potentials were shown to simulate well the results including higher hole-line contributions up to $3 \sim 4$ ρ_0 [16,17], ρ_0 being normal density. Here, G-matrix calculations are performed in nuclear matter, and G-matrix interactions are represented in coordinate space to construct nucleus-nucleus folding potentials [12].

In the same way as [6,7], the analyses for the ^{16}O+^{16}O elastic scattering at an incident energy per nucleon $E_{in}/A = 70$ MeV are performed. The MPP strengths ($g_P^{(3)}$ and $g_P^{(4)}$) and the TNA parameters (V_0 and η) are determined to reproduce the scattering data using the G-matrix folding potential derived from ESC+MPP+TNA and nuclear-matter energy at saturation density. The calculated angular distributions of ^{16}O+^{16}O scattering are insensitive to the TNA parameters. Namely, it is essential in our approach that they are substantially determined by the MPP repulsive contributions in high density region [13]. On the other hand, they are not so dependent on a ratio of contributions of triple and quartic pomeron exchanges, and we can find various combinations of $g_P^{(3)}$ and $g_P^{(4)}$ reproducing the data equally well.

The chosen parameter sets are listed in Table 1, where MPa and MPb sets were used also in [7]. As stated in [6], the analyses of the experimental cross sections of the process $pp \to pX$ gives rise to rough estimations $g_P^{(3)} = 1.95 \sim 2.6$ and $g_P^{(4)} = 33 \sim 228$ [18,19]. In the case of MPa, the $g_P^{(3)}$ value is within the estimated range, and the $g_P^{(4)}$ is of a permissible minimum value. MPa$^+$ is specified by having a fairly larger value of $g_P^{(4)}$ than MPa. On the other hand, MPb has no quartic component ($g_P^{(4)} = 0$). As found in Eq.(2), the contributions from triple and quartic components are proportional to ρ and ρ^2, respectively. Therefore, the latter contribution play a remarkable role to stiffen the EoS in high density region.

In Fig. 1, we show the energy curves of symmetric nuclear matter (lower curves) and neutron matter (upper curves), namely binding energy per nucleon (E/A) as a function of density ρ. Solid, dashed and dotted curves are obtained by MPa, MPa$^+$ and MPb sets, respectively. The box in the figure shows the area where nuclear saturation is expected to occur empirically. Then, saturation densities and minimum values of E/A curves by these sets turn out to be nicely close to the empirical value. In order to derive the compressibility K, the saturation curve is fitted by a function $E/A = a\rho + b\rho^\gamma$ at $0.07 < \rho < 0.4$ fm^{-3}. The obtained values of K are 283, 313 and 254 MeV for MPa, MPa$^+$ and MPb, respectively, where the saturation points are the same value of $\rho_0 = 0.154$ fm^{-3}.

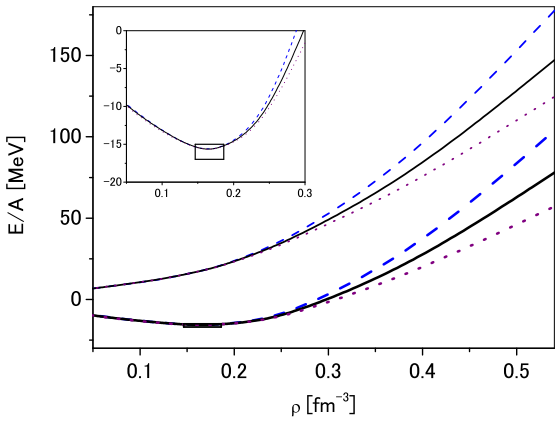

Fig. 1. Energy per particle (E/A) as a function of nucleon density ρ. Upper (lower) curves are for neutron matter (symmetric matter). Solid, dashed and dotted curves are for MPa, MPa$^+$ and MPb, respectively. The box shows the empirical value. The inset shows a zoom of the region around the saturation point.

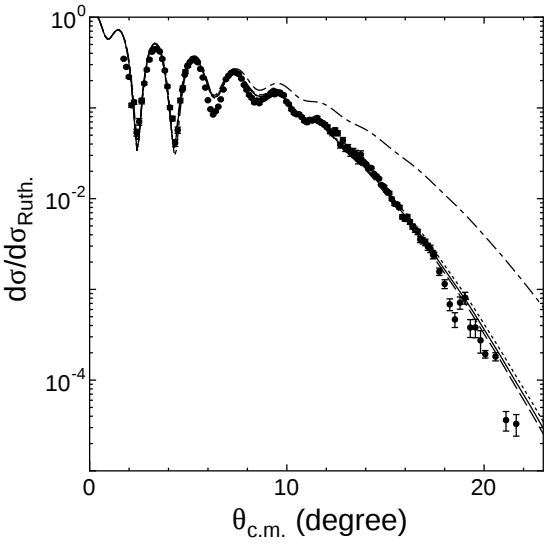

Fig. 2. Differential cross sections for ^{16}O+^{16}O elastic scattering at $E/A = 70$ MeV calculated with the G-matrix folding potentials. Solid, dashed and dotted curves are for MPa, MPa$^+$ and MPb, respectively. Dot-dashed curve is for ESC.

In Fig.2, the calculated results of the differential cross sections for the ^{16}O+^{16}O elastic scattering at $E/A = 70$ MeV are compared with the experimental data [20]. The corresponding ^{16}O+^{16}O double-folding potentials are shown in Fig.3. Here, the dot-dashed curves are obtained from ESC, and the angular distribution deviates substantially from the data. Solid, dashed and dotted curves are for MPa, MPa$^+$ and MPb, respectively, which reproduce nicely the experimental data. Though a reduction factors N_W is often multiplied on the imaginary part in the folding model analyses [12], such a reduction factor is not needed in the present cases. In the double-folding model

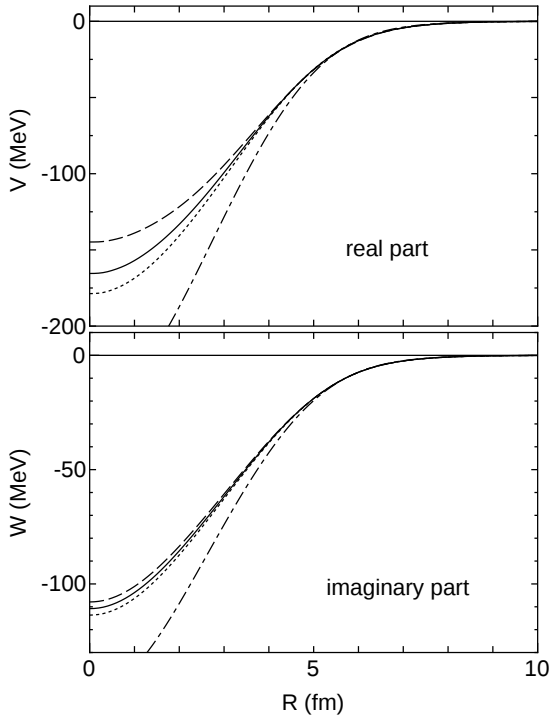

Fig. 3. Double-folding potentials for ^{16}O+^{16}O elastic scattering at $E/A = 70$ MeV. Solid, dashed and dotted curves are for MPa, MPa$^+$ and MPb, respectively. Dot-dashed curve is for ESC.

analyses, the most important is the validity of the frozen-density approximation (FDA). As shown in [13], MPP contributions from the density region higher than the normal density are decisively important for resultant angular distributions. Namely, valuable information of the EoS in high-density region can be obtained from double-folding potentials with FDA. The effect to include the quartic pomeron coupling has to appear in the difference between results for MPa/MPa$^+$ and MPb, but no meaningful effect can be found in the present analyses for nucleus-nucleus scattering.

It is instructive to compare our MPP with another model, for instance, the short-range repulsive term in the Urbana model IX (UIX) [21]. Because the strength of UIX is determined on the basis of variational calculations for nuclear systems, two-body correlations should be taken into account in deriving an effective two-body potential from a three-body potential for use of UIX in our G-matrix calculations. We estimate the effect of two-body correlations in the case of MPb with no quartic component, where correlation functions are extracted from the solutions of G-matrix equation in nuclear matter. The G-matrix results from MPb without correlations are found to be very similar to the results including correlations, if the $g_P^{(3)}$ value in MPb is multiplied by about 1.5. Then, in comparison with the calculations including UIX instead of the MPP part in MPb, it turns out that the G-matrices in both cases give rise to similar results. Namely, the

Table 2. Parameters in Eq.(4)

	a_0	b_0	c_0	a_1	b_1	c_1
MPa	−234.8	643.8	1.86	66.41	490.1	2.40
MPa$^+$	−186.1	814.9	2.23	76.36	808.7	2.83
MPb	−376.4	639.0	1.47	36.46	334.8	1.89

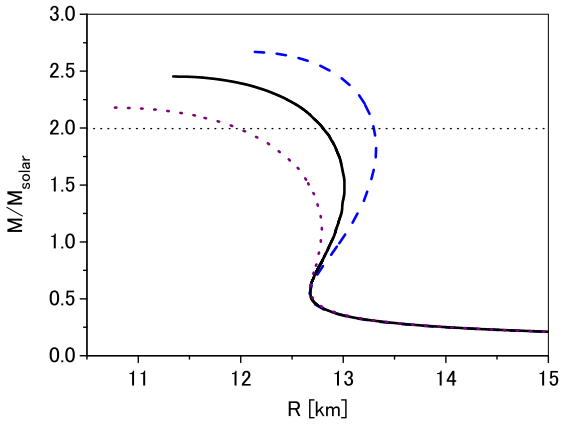

Fig. 4. Neutron-star masses as a function of the radius R. Solid, dashed and dotted curves are for MPa, MPa$^+$ and MPb, respectively.

strengths of three-body repulsions of MPb and UIX are rather similar to each other.

2.3 neutron star mass

From the G-matrix calculations, we obtain the energy per nucleon E/A as a function of density ρ. The E/A curve in nuclear matter with neutron density ρ_n and proton density ρ_p is parameterized as

$$E/A = (1-\beta)(a_0\rho + b_0\rho^{c_0}) + \beta(a_1\rho + b_1\rho^{c_1}) \qquad (4)$$

with $\beta = 1 - 2x$, $x = \rho_p/\rho$ and $\rho = \rho_n + \rho_p$.

Energy density, chemical potential and pressure are obtained from Eq.(4) as a function of ρ and β. Assuming a mixed matter of n, p, e^- and μ^- in chemical equilibrium, we solve the TOV equation for the hydrostatic structure of a spherical nonrotating star. The obtained mass-radius relations of neutron stars are demonstrated in Fig.4. Solid, dashed and dotted curves are for MPa, MPa$^+$ and MPb, respectively. The EoS's in these cases are found to be stiff enough to give $2M_\odot$. The difference between MPa (MPa$^+$) and MPb is due to the quartic-pomeron exchange term included in the formers. The strengths of the effective two-body interaction derived from quartic-pomeron exchanges are proportional to ρ^2, and the contribution become sizeable in the high-density region, making the maximum mass large. The above differences appear significantly in the inner regions of ^{16}O+^{16}O double-folding potentials in the inner region, though they cannot be seen in the cross sections Fig.2.

3 hyperon mixing in neutron stars

3.1 YN interaction

ESC gives potentials in $S=-1$ (ΛN, ΣN) and $S=-2$ (ΞN, $\Lambda\Lambda$ and $\Lambda\Sigma$) channels, being designed consistently with various data of YN scattering and hypernuclei. Then, the most important is to test the MPP+TBA parts in channels including hyperons. While MPP is defined universally in all baryon channel, TBA is introduced phenomenologically in nucleon channels, and not defined in YN channels. Then, we should determine the strength of TBA in each YN channel so as to reproduce the related hypernuclear data. Fortunately, the present version of ESC reproduces well the basic features of $S=-1$ and $S-2$ systems obtained from experimental data. This means that MPP contributions in YN channels as well as those in NN channels are canceled substantially by TBA contributions at normal density region. Then, it is confirmed that the hypernuclear data are reproduced by ESC+MPP+TBA as well as ESC by choosing TBA in a YN channel equally to that in a NN channel. One should notice, however, that the validity of this simple choice of TBA is rather accidental. There still remains ambiguities in the parameter fitting of ESC due to lack of experimental data in YN channels. When another parameter set of ESC is used, it is likely that TBA in a YN channel is different from TNA in a NN channel.

In the case of ΛN case, such an assumption can be tested in detail by using the experimental data of Λ hypernuclei: We calculate ΛN G-matrices in symmetric nuclear matter including a single Λ hyperon. In Table 3 we show the potential energies U_Λ for a zero-momentum Λ and their partial-wave contributions in $^1S_0$, $^3S_1$, P and D states at normal density ρ_0 (k_F=1.35 fm^{-1}). It is noted that reasonable Λ binding energies are obtained in the cases of MPa, MPa$^+$, MPb and ESC. The former three results including MPP+TBA are found to be similar to the ESC result, because MPP and TBA contributions are cancelled out substantially in normal density region in spite of remarkable difference in higher density region. One should be careful for comparing these values of $U_\Lambda(\rho_0)$ with the depth $U_{WS}\sim -30$ MeV of the Λ Woods-Saxon (WS) potential suitable to the data of Λ hypernuclei. In the cases of using the Skyrme-type ΛN interactions [22] or the Λ energy densities [23] in calculations of B_Λ values in finite systems, the derived Λ-nucleus potentials are more or less similar to the WS form and the potential depths have good correspondence to the U_{WS} value. On the other hand, in [7] Λ binding energies in finite systems were calculated systematically with the Λ-nucleus folding potentials derived from finite-range G-matrix interactions $G_{\Lambda N}(r;k_F)$ for MPa and ESC, and the experimental data were reproduced nicely. The similar result is obtained for MPb, while that for MPa$^+$ is a little smaller than the data. In these cases, the forms of Λ-nucleus folding potentials are considerably different from the WS form, and then the potential depths are not simply compared with the WS one. The reason why we use the G-matrix folding potentials for hyperon-nucleus interactions is because nucleon-nucleus and nucleus-nucleus scattering phenomena are quite successfully reproduced with G-matrix folding models. In [7], such an analysis was used to extract the three-body repulsive effect from the nucleus-nucleus scattering observable. For consistency in our approach, we use the G-matrix folding procedures for hyperon-nucleus potentials.

Table 3. Values of U_Λ at normal density and partial wave contributions for MPa, MPa$^+$, MPb and ESC (in MeV). Values specified by P and D give sum of (S,J) contributions.

	$^1S_0$	$^3S_1$	P	D	U_Λ
MPa	−13.6	−25.9	4.1	−2.7	−38.1
MPa$^+$	−13.3	−25.1	4.3	−2.7	−36.9
MPb	−13.6	−26.0	4.1	−2.7	−38.3
ESC	−13.6	−25.3	1.1	−1.6	−39.4

Table 4. Values of U_Σ at normal density and partial wave contributions for MPa, MPa$^+$, MPb and ESC (in MeV). Values specified by P and D give sum of (S,J) contributions.

		$^1S_0$	$^3S_1$	P	D	U_Σ
MPa	$T=1/2$	10.7	−23.1	−1.4	−1.0	
	$T=3/2$	−13.3	30.4	0.1	−0.9	1.5
MPa$^+$	$T=1/2$	10.6	−21.3	−1.4	−1.0	
	$T=3/2$	−13.3	30.4	0.2	−0.9	3.4
MPb	$T=1/2$	10.6	−23.2	−1.4	−1.0	
	$T=3/2$	−13.3	30.3	0.1	−0.9	1.3
ESC	$T=1/2$	10.9	−21.6	−2.5	−0.7	
	$T=3/2$	−13.5	31.0	−2.1	−0.2	1.3

In Table 4 we show the potential energies $U_\Sigma(\rho_0)$ for a zero-momentum Σ and their partial-wave contributions for MPa, MPa$^+$, MPb and ESC. As well as the cases of $U_\Lambda(\rho_0)$, the results for MPa, MPa$^+$ and MPb are similar to the ESC result because of cancellations of MPP and TBA contributions in normal density region. It should be noted here that the strongly repulsive contributions in $T=3/2$ $^3S_1$ and $T=1/2$ $^1S_0$ states are due to the Pauli-forbidden effects in these states, being taken into account by strengthening the pomeron coupling in the ESC08 modeling. Especially, Σ^- potentials in neutron matter become strongly repulsive owing to $T=3/2$ $^3S_1$ contributions. From the experimental data of Σ^- hypernuclear production, the Σ-nucleus potential is suggested to be strongly repulsive. It was shown that the experimental K^+ spectra of ^{28}Si(π^-,K^+) reaction were reproduced using the repulsive Woods-Saxon (WS) potential with the strength $U_{WS}=20\sim 30$ MeV [24]. It is meaningful to compare the WS potential with the Σ potential obtained from ΣN G-matrices for the Σ particle with positive energy in nuclear matter. Then, the latter is found to be repulsive comparably to the former in the Σ^- energy region related to the above (π^-,K^+) reaction. It is an interesting subject in future to analyze the (π^-,K^+) reaction data with use of the Σ-nucleus G-matrix folding potentials.

3.2 Hyperonic nuclear matter and EoS

We derive the EoS of baryonic matter composed of nucleons ($N = n, p$) and hyperons ($Y = \Lambda, \Sigma^-, \Xi^-$). A single particle potential of B particle in B' matter is given by

$$U_B(k) = \sum_{B'} U_B^{(B')}(k) = \sum_{B'} \sum_{k', k_F^{(B')}} \langle kk'|G_{BB',BB'}|kk'\rangle \quad (5)$$

with $B, B' = N, Y$. Here, spin isospin quantum numbers are implicit. The energy density is given by

$$\varepsilon = \varepsilon_{mass} + \varepsilon_{kin} + \varepsilon_{pot} = 2\sum_B \int_0^{k_F^B} \frac{d^3k}{(2\pi)^3} \left\{ M_B + \frac{\hbar^2 k^2}{2M_B} + \frac{1}{2} U_B(k) \right\} \quad (6)$$

Then, we have

$$\int_0^{k_F^B} \frac{k^2 dk}{\pi^2} U_B^{(B')}(k) = \int_0^{k_F^{B'}} \frac{k^2 dk}{\pi^2} U_{B'}^{(B)}(k)$$

.

Considering $\rho_B = \frac{(k_F^B)^3}{3\pi^2}$

$$\frac{\partial}{\partial \rho_B} \mathcal{U}_B^{(B')} = U_B^{(B')}(k_F^B) + \int_0^{k_F^B} \frac{k^2 dk}{\pi^2} \frac{\partial U_B^{(B')}(k)}{\partial \rho_B} \quad (7)$$

The second term leads to the rearrangement contribution.

The baryon number density is given as $\rho = \sum_B \rho_B$, ρ_B being that for component B. The chemical potentials μ_B and pressure P are expressed as

$$\mu_B = \frac{\partial \varepsilon}{\partial \rho_B} , \quad (8)$$

$$P = \rho^2 \frac{\partial(\varepsilon/\rho)}{\partial \rho_B} = \sum_B \mu_B \rho_B - \varepsilon . \quad (9)$$

Here, the two approximations are made for the energy density: (1) Hyperonic energy densities including Λ, Σ^- and Ξ^- are obtained from calculations of $n+p+\Lambda$, $n+p+\Sigma^-$ and $n+p+\Xi^-$ systems, respectively. (2) The parabolic approximation is used to treat asymmetries between n and p in $n+p$ sectors. Then, the G-matrix equations are solved for YN pairs ($Y = \Lambda, \Sigma$) specified by isospin quantum numbers, where the ΛN-ΣN coupling terms are treated exactly. The obtained isospin-represented YN G-matrices are transformed into those for Λn, Λp, $\Sigma^- n$ and $\Sigma^- p$. The corresponding terms for ΞN pairs are done approximately as mentioned later.

Calculated values of energy densities are fitted by the following analytical parameterization:

$$\varepsilon_{pot}(\rho_n, \rho_p, \rho_\Lambda, \rho_\Sigma, \rho_\Xi) = E_N \rho_N + (E_\Lambda + E_{\Lambda\Lambda})\rho_\Lambda + E_\Sigma \rho_\Sigma + E_\Xi \rho_\Xi \quad (10)$$

$$E_z = (1-\beta) f_z^{(0)} + \beta f_z^{(1)} \quad (11)$$

$$z = \Lambda, \Sigma, \Xi, \Lambda\Lambda$$

Table 5. Parameters of energy densities given by analytical forms Eqs.(13)∼(15).

	$a_{\Lambda 0}^{(0)}$	$a_{\Lambda 1}^{(0)}$	$b_{\Lambda 0}^{(0)}$	$b_{\Lambda 1}^{(0)}$	$c_\Lambda^{(0)}$
MPa	−343.4	82.30	1224.	1121.	2.288
MPa$^+$	−273.0	−73.75	1449.	3582.	2.695
MPb	−1191.	−449.2	1512.	912.1	1.246
	$a_{\Lambda 0}^{(1)}$	$a_{\Lambda 1}^{(1)}$	$b_{\Lambda 0}^{(1)}$	$b_{\Lambda 1}^{(1)}$	$c_\Lambda^{(1)}$
MPa	−208.4	−66.90	1124.	2204.	2.555
MPa$^+$	−262.7	−228.6	1184.	2902.	2.338
MPb	−1133.	−184.5	1540.	576.8	1.273
	$a_{\Sigma 0}^{(0)}$	$a_{\Sigma 1}^{(0)}$	$b_{\Sigma 0}^{(0)}$	$b_{\Sigma 1}^{(0)}$	$c_\Sigma^{(0)}$
MPa	−252.8	−261.7	699.2	992.8	1.591
MPa$^+$	−72.87	−80.57	666.6	1531.	2.254
MPb	−847.0	−594.3	1174.	930.3	1.184
	$a_{\Sigma 0}^{(1)}$	$a_{\Sigma 1}^{(1)}$	$b_{\Sigma 0}^{(1)}$	$b_{\Sigma 1}^{(1)}$	$c_\Sigma^{(1)}$
MPa	105.3	104.1	945.5	1447.	2.645
MPa$^+$	102.8	39.74	967.0	2628.	2.777
MPb	−84.92	−30.89	687.3	557.6	1.613
	$a_{\Lambda\Lambda 0}^{(1)}$	$a_{\Lambda\Lambda 1}^{(1)}$	$b_{\Lambda\Lambda 0}^{(1)}$	$b_{\Lambda\Lambda 1}^{(1)}$	$c_{\Lambda\Lambda}^{(1)}$
MPa	−1.185	−69.88	−20.17	612.2	2.272
MPa$^+$	−2.294	−33.30	−44.02	1090.	2.885
MPb	7.449	−256.9	−232.6	2325.	1.869

where $\beta = (1-2x_p)^2$ with $x_p = \rho_p/\rho_N$ and $\rho_N = \rho_n + \rho_p$. E_N means E/A given by Eq.(4). Expressions of $f_z^{(i)}$ with $i = 0, 1$ are given as

$$f_y^{(i)} = A_y^{(i)} \rho_N + B_y^{(i)} \rho_N^{c_y^{(i)}} \quad (12)$$

$$A_y^{(i)} = a_{y0}^{(i)} + a_{y1}^{(i)} x_Y \quad (13)$$

$$B_y^{(i)} = b_{y0}^{(i)} + b_{y1}^{(i)} x_Y \quad (14)$$

where $x_Y = \rho_Y/\rho_N$ with $Y = \Lambda$, Σ, Ξ, and $y = \Lambda$, Σ, Ξ, $\Lambda\Lambda$. Here, Λ, Σ, Ξ, $\Lambda\Lambda$ denote contributions from $N\Lambda$, $N\Sigma^-$, $N\Xi^-$ $\Lambda\Lambda$ interactions, respectively. The values of fitted parameters are listed in Table 5, where $\Lambda\Lambda$ ($i = 0$) parts are omitted because of their negligible effects in the EoS. In this work, $\Sigma^-\Sigma^-$ and $\Xi^-\Xi^-$ interactions are not taken into account, for which there is no experimental information.

Let us derive the EoS of neutron-star matter composed of n, p, e^-, μ^-, Λ, Σ^- and Ξ^-. The equilibrium conditions are summarized as follows: (1) chemical equilibrium conditions,

$$\mu_n = \mu_p + \mu_e \quad (15)$$

$$\mu_\mu = \mu_e \quad (16)$$

$$\mu_\Lambda = \mu_n \quad (17)$$

$$\mu_{\Sigma^-} = \mu_n + \mu_e \quad (18)$$

$$\mu_{\Xi^-} = \mu_n + \mu_e \quad (19)$$

(2) charge neutrality,

$$\rho_p = \rho_e + \rho_\mu + \rho_{\Sigma^-} + \rho_{\Xi^-} \quad (20)$$

(3) baryon number conservation,

$$\rho = \rho_n + \rho_p + \rho_\Lambda + \rho_{\Sigma^-} + \rho_{\Xi^-} \quad (21)$$

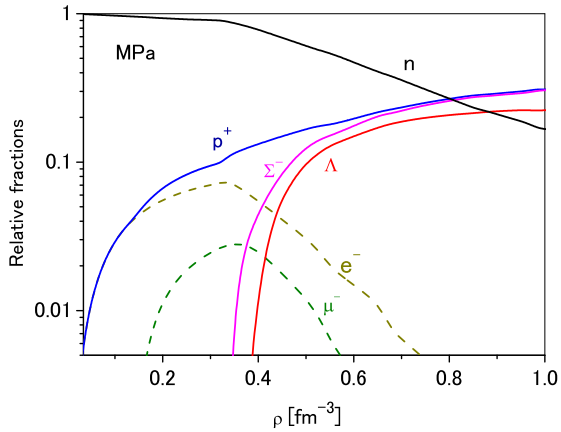

Fig. 5. Composition of hyperonic neutron-star matter for MPa.

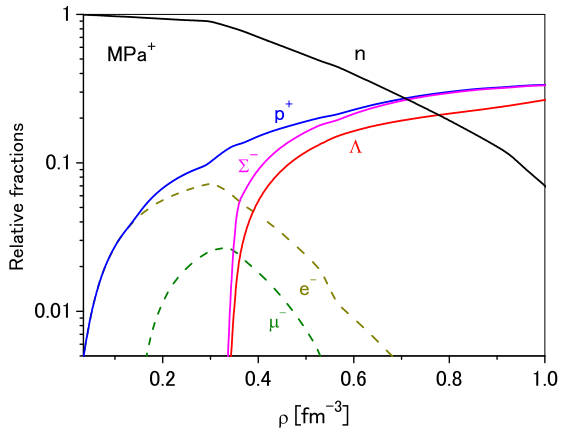

Fig. 6. Composition of hyperonic neutron-star matter for MPa^+.

When the analytical expressions (10)∼(14) are substituted into the chemical potentials (8), the chemical equilibrium conditions (15)∼(19) are represented as equations for densities ρ_a ($a = n$, p, e^-, μ^-, Λ, Σ^-, Ξ^-). Then, equations (15)∼(21) can be solved iteratively.

In this subsection, let us show the results obtained without Ξ^- mixing. In Fig. 5, Fig. 6 and Fig. 7, the matter compositions are shown in the cases of MPa, MPa^+ and MPb, respectively. As the MPP repulsions become strong from MPb to MPa^+, hyperon components become large. Increasing of hyperon components are found to be covered by decreasing of components of n, e^- and μ^-.

Pressures (9) are obtained from determined values of densities and chemical potentials. In Fig. 8, the calculated values of pressure P are drawn as a function of baryon density ρ. Thick (thin) curves are with (without) hyperon mixing. Solid, dashed and dotted curves are for MPa, MPa^+ and MPb.

Using the EoS of hyperonic nucleon matter, we solve the TOV equation to obtain the mass and radius of neu-

Fig. 7. Composition of hyperonic neutron-star matter for MPb.

Fig. 8. Pressure P as a function of baryon density ρ. Thick (thin) curves are with (without) hyperon mixing. Solid, dashed and dotted curves are for MPa, MPa^+ and MPb.

tron stars. The EoS's for MPa, MPa^+ and MPb are used $\rho > \rho_0$. Below ρ_0 we use the EoS of the crust obtained in [25,26]. Then, the EoS's for $\rho > \rho_0$ and $\rho < \rho_0$ are connected smoothly. The behavior of mass-radius curve of a neutron star in $\rho_0 \sim 2\rho$ region (below hyperon-onset densities) is considerably affected by the matching density. The above value of the matching density is chosen so that the winding behavior of the mass-radius curve in this region becomes as small as possible. Though there is no physical reason for this choice, the problem in $\rho_0 \sim 2\rho$ region is not related to the EoS and the mass-radius relations in higher-density region, which are of our concern in this work. In Fig. 9 (Fig. 10), neutron-star masses are drawn as a function of radius R (central density ρ_c), where solid, dashed and dotted curves are for MPa, MPa^+ and MPb, respectively. Calculated values of maximum masses for MPa^+, MPa and MPb are $2.07M_\odot$, $1.94M_\odot$ and $1.83M_\odot$, respectively, being smaller by $0.61M_\odot$, $0.51M_\odot$ and $0.35M_\odot$, than the values without hyperon mixing. Al-

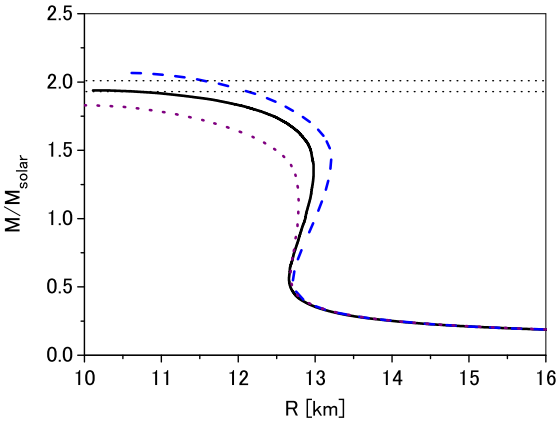

Fig. 9. Neutron-star masses as a function of the radius R. Solid, dashed and dotted curves are for MPa, MPa$^+$ and MPb. Two dotted lines show the observed mass $(1.97 \pm 0.04)M_\odot$ of J1614-2230.

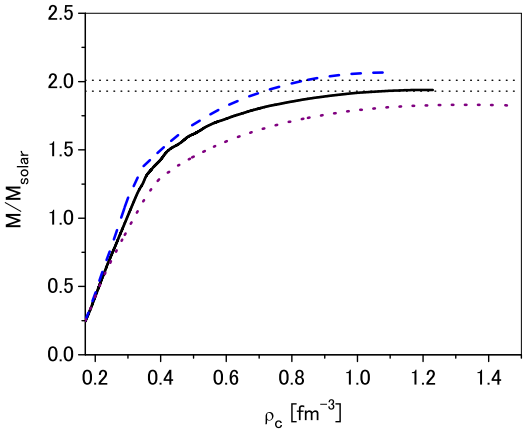

Fig. 10. Neutron-star masses as a function of the central density ρ_c. Solid, dashed and dotted curves are for MPa, MPa$^+$ and MPb. Two dotted lines show the observed mass $(1.97 \pm 0.04)M_\odot$ of J1614-2230.

though the universal repulsion works to raise the maximum mass, the hyperon mixing also is enhanced by it so that the maximum mass is reduced. This means that the universal repulsion cannot raise the maximum mass without limit. The maximum mass for MPb is considerably smaller than the observed value of $\sim 2M_\odot$. On the other hand, those for MPa and MPa$^+$ reach to this value owing to the four-body repulsive contributions. If a neutron star with far heavier mass than $2M_\odot$ is observed in future, it may be difficult to reproduce such a heavy mass in the present modeling for hyperon mixing.

In our calculations, the causality conditions at very high density are violated in the case of using MPa and MPa$^+$, and not in MPb case. Then, we adopt the approximation where the EoS is replaced by the causal EoS above this density in the same way as the treatment in [27]. The critical density for MPa and MPa$^+$, sound speeds being over the speed of light, is obtained as 1.2 and 1.1 fm^{-3}, respectively. The masses $M/M_\odot$ take the maximum values at ~ 1.23 and ~ 1.10 fm^{-3} in the case of MPa and MPa$^+$, respectively. The critical density for the violation of causality condition is almost the same as the density giving the maximum mass in these cases. Therefore, the obtained maximum masses are not so dependent on the above approximation. On the other hand, the causality condition is violated significantly in the corresponding result without hyperon mixing.

Table 6. Values of U_Ξ at normal density and partial wave contributions for MPa and ESC (in MeV). Values specified by P give sum of (S, J) contributions.

		$^1S_0$	$^3S_1$	P	U_Ξ
MPa	$T=0$	1.0	−8.1	1.5	
	$T=1$	9.7	−12.0	1.1	−6.7
ESC	$T=0$	1.1	−8.0	0.9	
	$T=1$	10.7	−10.8	−0.7	−6.8

3.3 ΞN interaction and Ξ^- mixing

Experimental information for ΞN interactions can be obtained from emulsion events of simultaneous emission of two Λ hypernuclei (twin Λ hypernuclei) from a Ξ^- absorption point. The Ξ^- produced by the (K^-, K^+) reaction is absorbed into a nucleus (^{12}C, ^{14}N or ^{16}O in emulsion) from some atomic orbit, and by the following $\Xi^- p \to \Lambda\Lambda$ process two Λ hypernuclei are produced. Then, the energy difference between the initial Ξ^- state and the final twin Λ hypernuclei gives rise to the binding energy B_{Ξ^-} between Ξ^- and the nucleus. Two events of twin Λ hypernuclei (I) [28] and (II) [29] were observed in the KEK E176 experiment. These events were interpreted to be reactions of Ξ^- captured from the $2P$ state in ^{12}C, though another possibility cannot be ruled out. In [30], the strength of the ΞN interaction was fitted according to this interpretation. Recently the new event (III) [15] has been observed in the KEK E373 experiment, as the first clear evidence of a Ξ^- bound state. This event is uniquely identified as $\Xi^- + {}^{14}\mathrm{N} \to {}^{10}_{\Lambda}\mathrm{Be} + {}^{5}_{\Lambda}\mathrm{He}$, where ${}^{10}_{\Lambda}$Be is in an excited state. Assuming the Ξ^- capture from the $2P$ state in ^{14}N, the obtained value of Ξ^- binding energy $B_{\Xi^-}(2P)$ agrees nicely to the value predicted in [30].

Recently, it has been shown in [11] that the Ξ^- binding energies extracted from the above events can be reproduced well by the G-matrix interaction derived from ESC08c. In Table 6 we show the potential energies $U_\Xi(\rho_0)$ for a zero-momentum Ξ and their partial-wave contributions for MPa and ESC. As well as the cases of Λ and Σ, the result for MPa is similar to that for ESC because of cancellations of MPP and TBA contributions in normal density region.

Now, we derive ΞN G-matrices in nuclear matter composed of $n + p + \Xi^-$ with ESC. ΞN sectors in ESC are

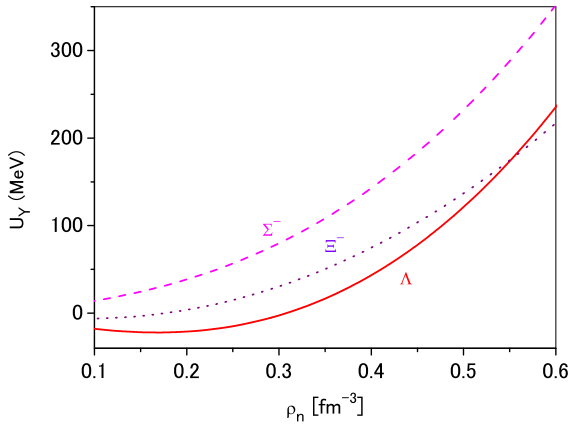

Fig. 11. Single particle potentials U_Y of $Y = \Lambda, \Sigma^-, \Xi^-$ for MPa in neutron matter as a function of neutron density ρ_n with $\rho_Y/\rho_n = 0.1$.

of complicated structure. For instance, ΞN channels in $T = 1$ state couples to $\Lambda\Sigma$ and $\Sigma\Sigma$ channels together with tensor coupling. For simplicity, we introduce an approximation to replace them by ΞN-ΞN single-channel potentials, which are determined so as to simulate the results by coupled-channel G-matrix calculations at normal-density. This approximation is for the sake of avoiding difficulties to solve the G-matrix equations with complicated coupling structures. For such a G-matrix equation, we have no good convergence for iterations in high-density region. It is our future problem to develop some technique to perform accurate calculations in such a case. However, the effects of Ξ mixing to the stiffness of EoS and the mass-radius relation of neutron stars may be not so large in the cases of including MPP contributions which dominate the energy densities in high-density region.

Calculations for MPa are performed, including MPP+TBA parts also in ΞN channels. In Fig.11, we compare calculated single particle potentials $U_Y^{(n)}(k = 0)$ with $Y = \Lambda, \Sigma^-, \Xi^-$ in neutron matter defined by Eq.(7), where they are given as a function of neutron density ρ_n in the case of $\rho_Y/\rho_n = 0.1$. The Ξ^- potential turns out to be less repulsive than the Σ^- potential.

The reason why the Σ^- potential is so repulsive is because of the Pauli-forbidden effect in the $^3S_1$ $T = 3/2$ state. As mentioned before, however, our Σ^- potential is less repulsive in comparison with the value $U_{\Sigma^-} \sim +30$ MeV assumed in the relativistic mean field models [31,32, 33]. This is the reason why the onset density of Σ^- is not so high in our EoS.

The values of fitted parameters for Ξ^- energy densities are listed in Table 7.

In Fig. 12, the matter compositions are shown in the case of MPa. Here, the onset densities of Σ^-, Λ and Ξ^- are 0.32 fm^{-3}, 0.36 fm^{-3} and 0.62 fm^{-3}, respectively.

In Fig. 13, the calculated values of pressure P are drawn as a function of baryon density ρ for MPa. Dashed and Solid curves are with and without Ξ^- mixing, respectively. Dotted curve is without hyperon mixing.

In Fig. 14, neutron-star masses are drawn as a function of radius, where the dashed (solid) curve is obtained from the EoS with (without) the Ξ^- mixing. The values of maximum masses are $1.97M_\odot$ and $1.94M_\odot$ in the cases of dashed and solid curves. Thus, the maximum mass is hardly changed, though Σ^- and Λ are replaced by Ξ^- gradually with increase of baryon density as seen in Fig. 12. The reason is because the universal repulsions (MPP) work equally to Λ, Σ^- and Ξ^-, being dominant

Table 7. Parameters of Ξ^- energy densities given by analytical forms Eq.(13)∼(15) for MPa.

$a^{(0)}_{\Xi 0}$	$a^{(0)}_{\Xi 1}$	$b^{(0)}_{\Xi 0}$	$b^{(0)}_{\Xi 1}$	$c^{(0)}_{\Xi}$
−290.9	145.8	1112.	304.2	1.893
$a^{(1)}_{\Xi 0}$	$a^{(1)}_{\Xi 1}$	$b^{(1)}_{\Xi 0}$	$b^{(1)}_{\Xi 1}$	$c^{(1)}_{\Xi}$
−133.4	8.011	783.2	739.6	2.077

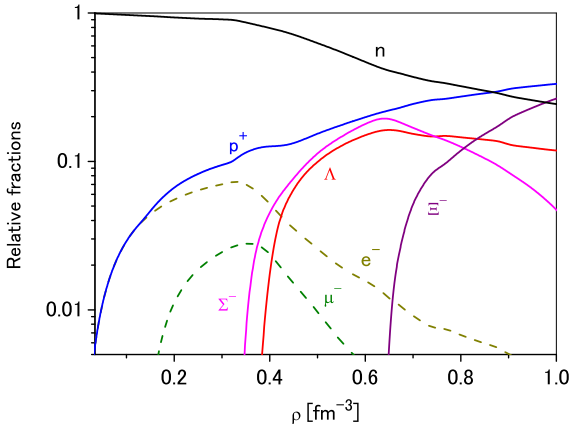

Fig. 12. Composition of hyperonic neutron-star matter for MPa.

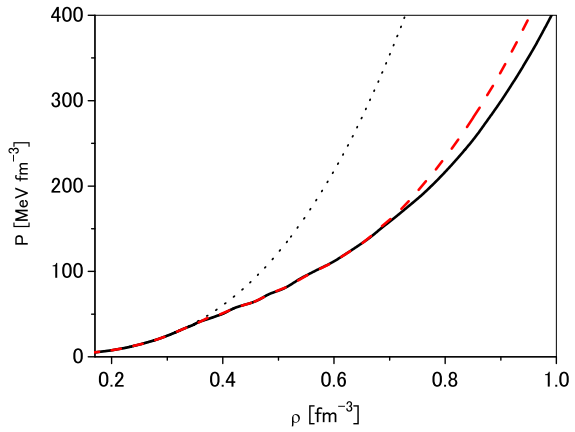

Fig. 13. Pressure P as a function of baryon density ρ. Dashed (solid) curves are with (without) Ξ^- mixing for MPa. Dotted curve is without hyperon mixing.

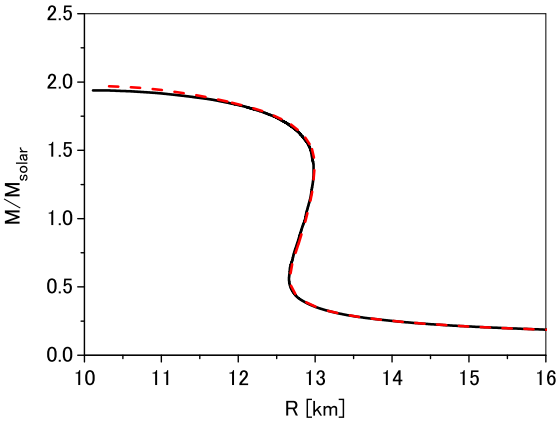

Fig. 14. Neutron-star masses as a function of the radius R derived from the hyperon-mixed EoS for MPa. Dashed (solid) curve is with (without) Ξ^- mixing.

contributions in high density region. The effect of Ξ^- mixing in Fig. 14 can be understood correspondingly by the difference between the EoS's with and without Ξ^- mixing in Fig. 13, where the former becomes harder than the latter in higher density region.

4 Conclusion

The existence of neutron stars with $2M_\odot$ gives a severe condition for the stiffness of EoS of neutron-star matter. Though the strong TNR can make the EoS stiff enough, the hyperon mixing in neutron-star matter brings about the remarkable softening of the EoS to cancel the TNR effect. As a possibility to avoid this serious problem, we introduce the universal repulsions working for YNN, YYN YYY as well as for NNN [5].

On the basis of the BB interaction model ESC, we introduce the universal three- and four-body repulsion MPP among baryons together with the phenomenological three-body attraction TBA. The strengths of MPP in nucleon channels are determined so as to fit the observed angular distribution of ^{16}O+^{16}O elastic scattering at $E_{in}/A = 70$ MeV with use of the G-matrix folding potential. The TBA parts are taken so as to assure the nuclear saturation property. Then, the stiff EoS of neutron-star matter is derived on the basis of terrestrial experiments, giving the large neutron-star mass over $2M_\odot$, when the hyperon mixing is not taken into account.

In order to study the effect of hyperon mixing to the EoS, it is necessary to use reliable interactions in channels including hyperons. The reliability of ESC in these channels have been confirmed by successful applications to analyses of hypernuclear phenomena. The MPP contributions are defined to exist universally in every baryonic system. Taking the remaining part TBA also universally, single particle potentials of Λ, Σ^- and Ξ^- are reproduced consistently with experimental data by using ESC+MPP+TBA interactions.

The EoS of hyperonic nuclear matter is obtained from ESC+MPP+TBA on the basis of the G-matrix approach, and the mass-radius relations of neutron stars are derived by solving the TOV equation. Though hyperon mixing leads to remarkable softening of the EoS, the stiffness is partially recovered owing to the MPP contribution. Quantitatively, in the case of MPb including only the three-body repulsion, the derived maximum mass is considerably smaller than $2M_\odot$. In order to reproduce $2M_\odot$, the decisive roles are played by the four-body repulsions included in MPa and MPa$^+$. The effective two-body interactions derived from the three- and four-body repulsions are proportional to ρ and ρ^2, respectively. The latter contribution in high density region is sufficient to stiffen the EoS enough to give $2M_\odot$. However, as the MPP repulsion becomes strong, the resultant softening effect of EoS becomes large. Namely, the neutron-star mass does not become far bigger than $2M_\odot$ with increase of the MPP repulsion: We can say that our three- and four-pomeron exchange model provides an upper limit $\sim 2M_\odot$ to the maximum mass of neutron stars with hyperon mixing.

The universality of the MPP repulsion not only applies to nucleons and hyperons but also baryon resonances (Δ_{33} etc.) and mesons as well. Therefore, the MPP repulsion prevents in general the softening of the EoS in the high-density region.

It is interesting to study the effect of Ξ^- mixing in addition to mixing of Λ and Σ^- on the basis of the reliable ΞN interaction model. The emulsion data of twin Λ hypernuclei indicate that the ΞN interaction is substantially attractive. Then, the Ξ^- binding energies are reproduced well by ESC. The EoS of neutron-star matter including hyperons (Λ, Σ^-, Ξ^-) is derived from ESC+MPP+TBA interactions. Though there appears considerable Ξ^- mixing in high density region, there is almost no effect on the maximum mass.

It should be noted that our conclusion for neutron stars is obtained essentially on the basis of terrestrial experiments for nuclear and hypernuclear systems without using ad hoc parameters to stiffen the EoS. It can be said, at least, that our approach contributes to one of possible solutions of the hyperon puzzle.

References

1. P.B. Demorest, T. Pennucci, S.M. Ransom, M.S.E. Roberts, and J.W. Hessels, Nature (London) **467**, (2010) 1081.
2. J. Antoniadis *et al.*, Science **340**, (2013) 6131.
3. M. Baldo, G.F. Burgio, and H.-J. Schulze, Phys. Rev. C**61**, (2000) 055801.
4. I. Vidana, A. Polls, A. Ramos, L. Engvik, and M. Hjorth-Jensen, Phys. Rev. C**62**, (2000) 035801.
5. S. Nishizaki, Y. Yamamoto, and T. Takatsuka, Prog. Theor. Phys. **105**, (2001) 607; **108**, (2002) 703.
6. Y.Yamamoto, T.Furumoto, N.Yasutake and Th.A.Rijken, Phys. Rev. C**88**, (2013) 022801.
7. Y.Yamamoto, T.Furumoto, N.Yasutake and Th.A.Rijken, Phys. Rev. C**90**, (2014) 045805.
8. Th.A. Rijken, M.M. Nagels, and Y. Yamamoto, Prog. Theor. Phys. Suppl. **185**, (2010) 14.

9. M.M. Nagels, Th.A. Rijken, and Y. Yamamoto, arXiv:1408.4825 (2014).
10. M.M. Nagels, Th.A. Rijken, and Y. Yamamoto, arXiv:1501.06636 (2015).
11. M.M. Nagels, Th.A. Rijken, and Y. Yamamoto, arXiv:1504.02634 (2015).
12. T. Furumoto, Y. Sakuragi, and Y. Yamamoto, Phys. Rev. C**79**, (2009) 011601(R); C**80**, (2009) 044614.
13. T. Furumoto, Y. Sakuragi, and Y. Yamamoto, Phys. Rev. C**90**, (2014) 041601(R).
14. I.E. Lagaris and V.R. Pandharipande, Nucl. Phys. A**359**, (1981) 349.
15. K. Nakazawa *et al.*, Prog. Theor. Exp. Phys. **2015**, 033D02.
16. H.Q.Song, M.Baldo, G.Giansiracusa and U.Lombardo, Phys. Rev. Lett. **81**, (1998) 1584.
17. M.Baldo, A.Fiasconaro, H.Q.Song, G.Giansiracusa and U.Lombardo, Phys. Rev. **C65**, (2002) 017303.
18. A.B. Kaidalov and K.A. Ter-Materosyan, Nucl. Phys. **74**, (1974) 471.
19. J.B. Bronzan and R.L. Sugar, Phys. Revs. D**16**, (1977) 466.
20. F. Nuoffer, et al., Nuovo Cimento A**111**, (1998) 971.
21. B.S. Pudliner, V.R. Pandharipande, J. Carlson, and R.B. Wiringa, Phys. Rev. Lett. **74**, (1995) 59.
22. Y. Yamamoto, H. Bandō and J. Žofka, Prog. Theor. Phys. **80**, (1988) 757 ; D.J. Millener, C.B. Dover and A. Gal, Phys. Rev. C**38**, (1988) 2700.
23. J. Cugnon, A. Lejeune and H.-J. Schulze, Phys. Rev. C**62**, (2000) 064308.
24. T. Harada and Y. Hirabayashi, Nucl. Phys. A**759**, (2005) 143.
25. G. Baym, A. Bethe, and C. Pethick, Nucl. Phys. A**175**, (1971) 225.
26. G. Baym, C.J. Pethick, and P. Sutherland, Astrophys. J.**170**, (1971) 299.
27. S. Gandolfi, J. Carlson, and Sanjjay Reddy, Phys. Rev. C**85**, (2012) 032801(R).
28. S. Aoki *et al.*, Prog. Theor. Phys. **89**, (1993), 493.
29. S. Aoki *et al.*, Phys. Lett. **B355**, (1995), 45.
30. M. Yamaguchi, K. Tominaga, Y. Yamamoto, and T. Ueda, Prog. Theor. Phys. **105**, (2001), 627.
31. S. Weissenborn, D. Chatterjee, and J. Schaffner-Bielich, Nucl. Phys. A**881**, (2012) 62.
32. I. Bednarek, P. Haensel, J.L. Zdunik, M. Bejger, and R. Mańka, Astronomy & Astrophysics A**157**, (2012) 543.
33. Wei-Zhou Jiang, Bao-An Li, and Lie-Wen Chen, Astrophys. J.**756**, (2012) 56.